

# Innovative fabrication of highly efficient CeO<sub>2</sub> ceramic nanomaterials for enhanced photocatalytic degradation of toxic contaminants under sunlight

Sahar Zinatloo-Ajabshir <sup>a,\*</sup>, Zohreh Mehrabadi <sup>b,\*\*</sup>, Hossein Khojasteh <sup>c</sup>, Fariborz Sharifianjazi <sup>d</sup>

<sup>a</sup> Department of Chemical Engineering, University of Bonab, P.O. Box. 5551395133, Bonab, Iran

<sup>b</sup> Department of Chemistry, Firoozabad Branch, Islamic Azad University, Firoozabad, Iran

<sup>c</sup> Scientific Research Center, Soran University, Kurdistan Region, Iraq

<sup>d</sup> Center for Advanced Materials and Structures, School of Science and Technology, The University of Georgia, Tbilisi, 0171, Georgia



## ARTICLE INFO

Handling Editor: Dr P. Vincenzini

### Keywords:

Sonochemical synthesis  
Cerium oxide nanoparticles  
Photocatalytic degradation  
Organic pollutants  
Glucose capping agent  
Visible light irradiation

## ABSTRACT

In this research, we report an innovative sonochemical technique for synthesizing cerium oxide (CeO<sub>2</sub>) nanoparticles utilizing glucose as a capping agent, significantly boosting their photocatalytic performance under visible light. Through meticulous optimization, our CeO<sub>2</sub> nanoparticles demonstrated exceptional degradation efficiencies: 97.2 % for Acid Red 14, 99.1 % for Captopril, 98.7 % for Malachite Green, and 98.3 % for Amiodipine, substantially outstripping performance metrics of commercial TiO<sub>2</sub> and untreated samples. Our kinetic analyses, based on the Langmuir-Hinshelwood model, indicated a superior rate constant of 0.0701 min<sup>-1</sup> for Acid Red 14 degradation—reflecting a stark enhancement over other catalysts tested. Furthermore, mechanistic insights revealed that the significant improvement in photocatalytic activity was predominantly due to the generation of hydroxyl radicals and effective utilization of electron vacancies, with the role of these reactive species validated by detailed scavenger tests. This enhancement in photocatalytic efficiency is attributed to the sonochemical synthesis paired with glucose modification, which optimizes the nanoparticles' surface characteristics crucial for reactivity. Moreover, the nanoparticles showcased remarkable stability and reusability, maintaining an 87.8 % degradation rate after 11 cycles, evidencing minimal loss in activity and underscoring their potential for long-term applications in environmental remediation. This study not only paves the way for the practical application of CeO<sub>2</sub> nanoparticles in pollutant degradation but also illustrates the broader applicability of sonochemically synthesized nanomaterials in sustainable environmental management, offering a promising solution to the challenge of complex organic pollutants in aquatic environments.

## 1. Introduction

Cerium oxide nanoparticles (nanoceria) are distinguished by their unique chemical properties, primarily composed of cerium dioxide and capable of fluctuating between Ce(III) and Ce(IV) oxidation states. These properties underpin their diverse applications in catalyzing chemical reactions and combating oxidative stress. The fluorite structure of CeO<sub>2</sub> nanoparticles is crucial, facilitating their roles in various catalytic and antioxidant processes [1,2].

Initially, cerium oxide found use in gas mantles, glass polishing, and as a decolorizing agent in glass manufacturing, capitalizing on its stability and optical properties [3–5]. The versatility of CeO<sub>2</sub> nanoparticles is utilized across various sectors. Industrially, they improve fuel cell

efficiency and reduce emissions, supporting cleaner energy and better air quality. Environmentally, they are integral to water purification technologies, effectively removing organic pollutants and heavy metals, demonstrating their potential for environmental remediation [6,7].

In healthcare, the antioxidant properties of cerium oxide nanoparticles provide therapeutic benefits, mimicking crucial enzymes to neutralize free radicals. This offers promising treatments for diseases linked to oxidative stress, such as Alzheimer's, Parkinson's, and various cancers. Their biomimetic capabilities are driving research into CeO<sub>2</sub> NP-based therapies that are more targeted and less toxic than traditional options [8–10].

The synthesis of CeO<sub>2</sub> NPs is a critical area of research, with methods such as hydrothermal synthesis, sol-gel processes, and precipitation

\* Corresponding author.

\*\* Corresponding author.

E-mail addresses: [s.zinatloo@ubonab.ac.ir](mailto:s.zinatloo@ubonab.ac.ir), [s.zinatloo@gmail.com](mailto:s.zinatloo@gmail.com) (S. Zinatloo-Ajabshir), [mehrabadi\\_2006@yahoo.com](mailto:mehrabadi_2006@yahoo.com) (Z. Mehrabadi).

reactions being refined to produce nanoparticles with specific sizes, shapes, and surface characteristics. These attributes directly influence their reactivity, stability, and suitability for different applications. The ongoing development of synthesis techniques aims to optimize these parameters for enhanced functionality and application specificity [11, 12].

The incorporation of sonochemistry and the use of ultrasound waves in the synthesis of cerium oxide nanoparticles represents a promising approach to overcome some of the limitations of traditional synthesis methods. By offering precise control over nanoparticle characteristics and potentially lower energy consumption, sonochemical synthesis contributes to the advancement of CeO<sub>2</sub> NPs research and application, paving the way for the development of more efficient, effective, and environmentally friendly nanomaterials [13,14].

Despite the promising attributes and applications of CeO<sub>2</sub> NPs, their deployment is not without challenges. Issues related to nanoparticle aggregation, stability under varying environmental conditions, and potential cytotoxicity are at the forefront of current research efforts. Addressing these challenges requires a multidisciplinary approach, combining insights from materials science, chemistry, biology, and environmental science to ensure the safe and effective use of CeO<sub>2</sub> NPs [15,16].

The potential of CeO<sub>2</sub> NPs is expanding in medical and environmental fields. Their capabilities are being explored in drug delivery, bio-imaging, and tissue regeneration, aiming to create less invasive and more effective treatments. Additionally, their role in sustainable energy and pollution control highlights the importance of nanotechnology in tackling global environmental challenges [17,18].

Cerium oxide nanoparticles are at the forefront of nanotechnology, demonstrating its potential to convert theoretical science into practical solutions for critical global issues. As research progresses, the full scope of CeO<sub>2</sub> nanoparticles' capabilities remains to be tapped, forecasting a future where their application in health, environmental protection, and technology continues to evolve and expand. This ongoing exploration and utilization signal a transformative era in nanotechnology, poised to significantly impact human health and environmental sustainability [19,20].

Nanotechnology's appeal stems from the enhanced catalytic, stability, and redox properties of materials like CeO<sub>2</sub> NPs compared to their bulk forms. Recognizing that nanoscale materials behave differently spurred advancements in their synthesis. Methods like hydrothermal synthesis, sol-gel processes, and later sonochemistry, enabled precise control over nanoparticle size, shape, and crystallinity, crucial for customizing their properties for specific applications [21,22].

Research into CeO<sub>2</sub> NPs expanded rapidly, exploring their potential in diverse fields. In catalysis, nanoceria showed promise in improving the efficiency of fuel cells and reducing emissions from vehicles. In biomedicine, its antioxidant properties opened avenues for therapeutic applications, including neuroprotection and cancer treatment. The environmental sector saw the potential of CeO<sub>2</sub> NPs in treating pollutants and in energy conversion technologies [17,23].

The historical trajectory of CeO<sub>2</sub> nanoparticles is documented extensively in scholarly articles, detailing their evolution from basic insights to sophisticated applications in biomedicine and environmental science. Beginning with Carl Walkey's work in 2014–2015, which highlighted their catalytic and antioxidant properties and the biological challenges for medical use, the research narrative progressed with Atul Dhall in 2018, who focused on synthesis methods and their implications for personalized medicine, emphasizing the importance of green synthesis for enhanced biocompatibility [4,21,24,25].

In 2020, Kshitij R. B. Singh and his team contributed a comprehensive review on the biosynthesis and wide-ranging biomedical applications of CeO<sub>2</sub> NPs, highlighting their pivotal role across various fields, including their significant impact on medicine and environmental protection. Furthermore, the contribution to the literature by authors in an IntechOpen book chapter delves into the structural nuances of CeO<sub>2</sub>

nanostructures, especially focusing on the crucial role of oxygen vacancies and their potential applications in technologies like solid oxide fuel cells (SOFCs) [3,26].

CeO<sub>2</sub> nanoparticles have a substantial surface area relative to their volume, enhancing their catalytic efficiency and interaction with various substances. They retain their crystalline structure under various conditions, demonstrating durability. Notably, their properties are size-dependent; smaller particles exhibit greater surface reactivity, crucial for catalytic and antioxidant functions. Quantum effects further modify their optical, electrical, and magnetic properties, expanding their potential uses [27,28].

The high surface area and presence of defects like oxygen vacancies endow CeO<sub>2</sub> NPs with exceptional catalytic activities, crucial for speeding up chemical reactions, including pollutant degradation and chemical synthesis. In biomedicine, their nanoscale properties enable enzymatic mimetic activities, offering potential in anti-inflammatory, neuroprotective, and anticancer therapies [29].

Despite their promise, CeO<sub>2</sub> nanoparticles encounter several challenges, including toxicity concerns and environmental impacts, such as potential oxidative stress in biological systems and bioaccumulation risks that necessitate thorough risk assessments. Additionally, manufacturing challenges such as achieving consistent nanoparticle characteristics are crucial for ensuring industrial scalability and effective application [30,31].

Addressing the challenges associated with CeO<sub>2</sub> nanoparticles requires a multidisciplinary approach to refine synthesis techniques, boost functionality, and ensure safety and sustainability. Progress in understanding their mechanisms and interactions is essential for developing new technologies and applications. This study builds on prior research by introducing a novel sonochemical approach using glucose as a capping agent, aiming to provide innovative solutions to environmental, energy, and biomedical challenges. Utilizing (NH<sub>4</sub>)<sub>2</sub>[Ce(NO<sub>3</sub>)<sub>6</sub>] as the cerium source, we explore the efficacy of both sodium hydroxide and ammonium hydroxide as precipitating agents, with a particular focus on the innovative use of ultrasonic waves to provide the necessary energy for the synthesis process. This sonochemical synthesis method not only enhances the reaction kinetics but also enables precise control over the nanoparticle characteristics, offering a greener and more efficient alternative to conventional synthesis techniques.

After a thorough optimization of the reaction conditions, the optimal nanoparticles were systematically characterized to elucidate their physicochemical properties. The characterization process involved a comprehensive analysis of the nanoparticles' size, morphology, crystallinity, and surface chemistry, providing valuable insights into how the use of glucose as a capping agent influences these parameters.

The culmination of our work lies in the application of these optimized CeO<sub>2</sub> NPs for the degradation of organic pollutants. Demonstrating a significant enhancement in catalytic performance, these nanoparticles exhibit a remarkable ability to break down various organic compounds, underscoring their potential as a sustainable solution for environmental remediation efforts. In a pioneering approach within the field of materials science, this study introduces the sonochemical synthesis of CeO<sub>2</sub> nanoparticles employing glucose as a capping agent for the first time. This innovative method leverages the unique properties of glucose to control the nanoparticle morphology and size, which significantly enhances their photocatalytic efficiency. The choice of glucose, a naturally derived capping agent, not only offers a green synthesis route but also optimizes the surface characteristics crucial for photocatalytic activity. This synergistic combination of sonochemistry and glucose has led to notable improvements in the photocatalytic efficiency of CeO<sub>2</sub> nanoparticles.

## 2. Experimental approach

### 2.1. Materials

For this research, NH<sub>4</sub>OH and NaOH were sourced from Merck Company and used as received, without additional purification. (NH<sub>4</sub>)<sub>2</sub>[Ce(NO<sub>3</sub>)<sub>6</sub>] was purchased from Sigma-Aldrich and served as the cerium source. D-glucose was employed as a capping agent and also purchased from Sigma-Aldrich. The deionized water used was produced by an ultra-pure water system (Smart-2-Pure, TKA Co., Germany). Acid Red 14 and Malachite Green were obtained from Alvan Co., Iran. Amlodipine and Captopril, provided in analytical grade by Merck Company, were used for photocatalytic experiments.

### 2.2. Surface characterization and particle analysis

The XRD analysis of the nanocomposites was performed using a Philips X-ray diffractometer equipped with Ni-filtered Cu K $\alpha$  radiation, with peak matching and phase identification aided by HighScore Plus software. The software matched the observed diffraction patterns to database entries using crystallographic parameters. The scanning rate was set to 1°/min over a 20 range of 20°–80°. The morphology and size of the nanoparticles were examined using a Philips XL-30ESM SEM. UV-Vis absorption spectra were acquired with a PerkinElmer Lambda2S spectrophotometer in the 200–800 nm range.

### 2.3. Synthesis of Cerium oxide nanoparticles

An ultrasonic probe device was operated with a power output of 100 W. First, 0.3g of the cerium source and glucose are dissolved in 60 mL of water using a magnetic stirrer. Following this, an ultrasonic probe is inserted into the container holding the solution and exposed to radiation for the duration specified in the table above, while an ammonia solution is added dropwise simultaneously. The pH is adjusted to 11. Subsequently, the mixture is centrifuged, and the precipitate is washed and then dried at 80–90 °C. Finally, the residue is calcined at 500 °C for 2 h (Schematic 1).

To identify the optimal conditions for synthesizing cerium oxide nanoparticles through sonication, the process was carried out under different conditions as detailed in Table 1. The investigation focused on several parameters, including the power (in Watts), duration of

**Table 1**

Summary of experimental parameters for the synthesis of cerium oxide nanoparticles via sonication.

Sample	Power (W)	Time (min)	Capping agent (mmol)	Precipitator type
1	60	10	1	NH <sub>3</sub> (25 %)
2	30	10	1	NH <sub>3</sub> (25 %)
3	90	10	1	NH <sub>3</sub> (25 %)
4	60	20	1	NH <sub>3</sub> (25 %)
5	60	5	1	NH <sub>3</sub> (25 %)
6	60	10	2	NH <sub>3</sub> (25 %)
7	60	10	0.5	NH <sub>3</sub> (25 %)
8 (blank)	0	0	1	NH <sub>3</sub> (25 %)
9 (blank)	60	10	—	NH <sub>3</sub> (25 %)
10	60	10	1	NaOH (0.1M)

sonication (in minutes), concentration of the capping agent (in millimoles), and the type of precipitator used.

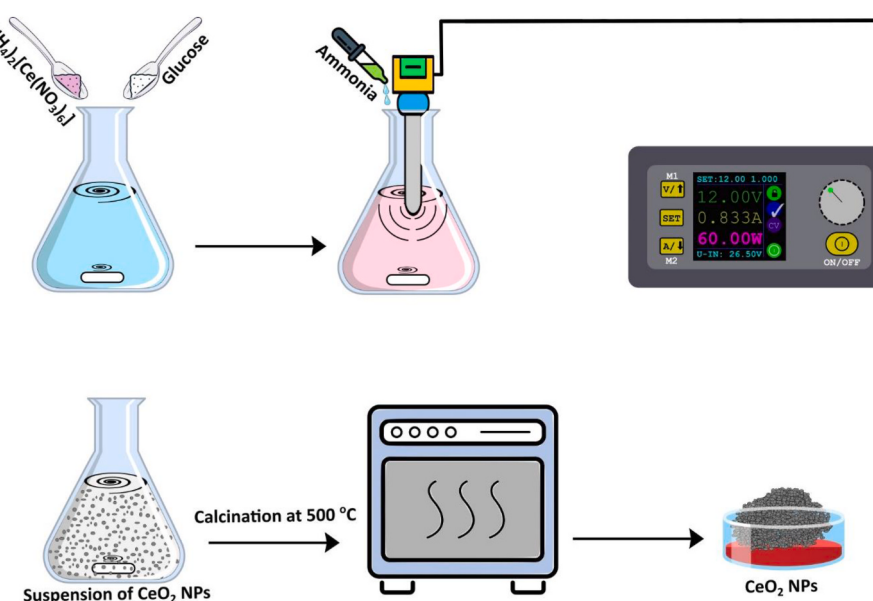
## 3. Results and discussion

### 3.1. Exploring the reaction parameters in morphology and particle size

Upon a detailed examination of the SEM images of cerium oxide nanoparticles synthesized at varying ultrasonic powers (Fig. 1), it appears that the use of 60 W presents the most favorable conditions, producing smaller and more uniformly distributed nanoparticles with reduced agglomeration. This observation is particularly evident in image c, where the average particle size is approximately 90 nm.

The dense nanoparticle population observed in Fig. 1a, at a 1  $\mu$ m scale, along with images b and c at a 200 nm scale, underscores a robust nucleation process, leading to the formation of numerous nanoparticles. These images suggest a delicate balance between nucleation and growth rates achieved at 60 W, facilitating the synthesis of nanoparticles that are less prone to clumping as opposed to the larger, more sparse particles produced at 30 W.

At the 30 W power setting, the SEM images, particularly image d at the 1  $\mu$ m scale and images e and f at the 200 and 100 nm scales, depict larger particles, implying a lower nucleation rate with a tendency for the particles to grow larger rather than to form new nucleation sites. This condition seems to be less ideal for the synthesis goals, as it leads to increased agglomeration.



Sch. 1. The process for the ultrasonic-assisted synthesis of CeO<sub>2</sub> NPs.

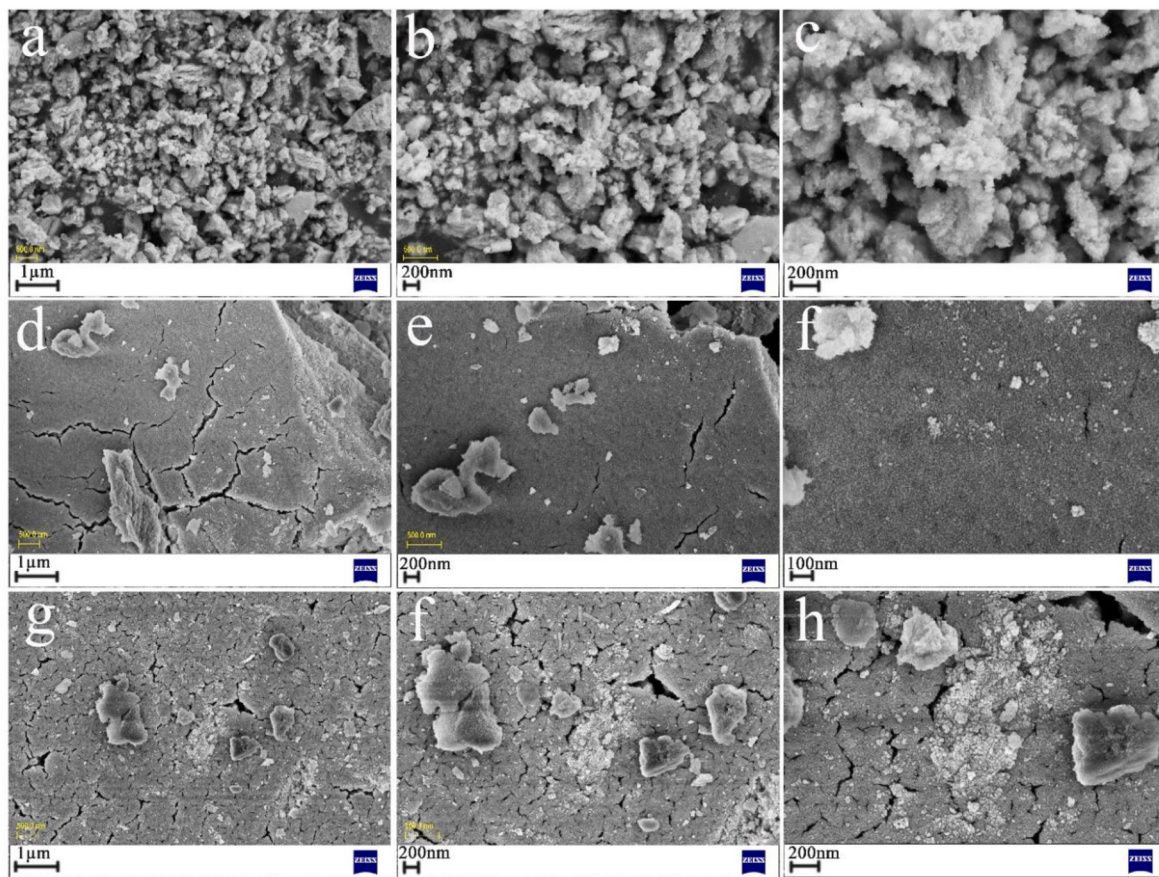


**Fig. 1.** FE-SEM analysis of CeO<sub>2</sub> NPs at 60 W (a–c), 30 W (d–f), and 90 W (g–h).

On the other hand, at a higher power of 90 W, SEM images g and h, although showing discrete particles at a microscale, do not align with the desired nanoparticle characteristics observed at the optimal 60 W setting. Here, the higher power may have introduced different dynamics in the growth and nucleation process, leading to a distinct particle morphology that may not be as beneficial for the application of interest [32].

Moving forward, the synthesis process appears to benefit from further optimization of other parameters such as sonication time, the concentration of the glucose capping agent, and the type of precipitator used. Modulating the sonication time could potentially decrease the tendency of nanoparticles to agglomerate, thereby increasing their individual stability. Adjusting the concentration of the glucose capping agent may offer a refined control over particle growth and could prevent excessive agglomeration. Lastly, exploring different precipitators might alter the pH and ionic strength of the solution, which in turn could significantly impact the final morphology of the nanoparticles. Such optimization is anticipated to further enhance the capabilities of CeO<sub>2</sub> nanoparticles for the degradation of organic pollutants, aligning with the specific objectives of the research.

Fig. 2 depicts the SEM images provide a comparative visualization of cerium oxide nanoparticles (CeO<sub>2</sub> NPs) synthesized under varying ultrasonic durations, specifically 20 min (images a–c) and 5 min (images d–f). The images a–c, corresponding to a 20-min ultrasonication, depict a landscape of CeO<sub>2</sub> NPs characterized by distinct separations and less surface coverage, suggesting that prolonged exposure to ultrasonication leads to overgrown particles with a propensity towards coarser and more distinct structures. This is especially apparent in image a (1 μm scale), where the fractured morphology implies substantial particle growth, potentially reducing the available reactive surface area.

Upon closer examination at the 200 nm and 100 nm scales (images b

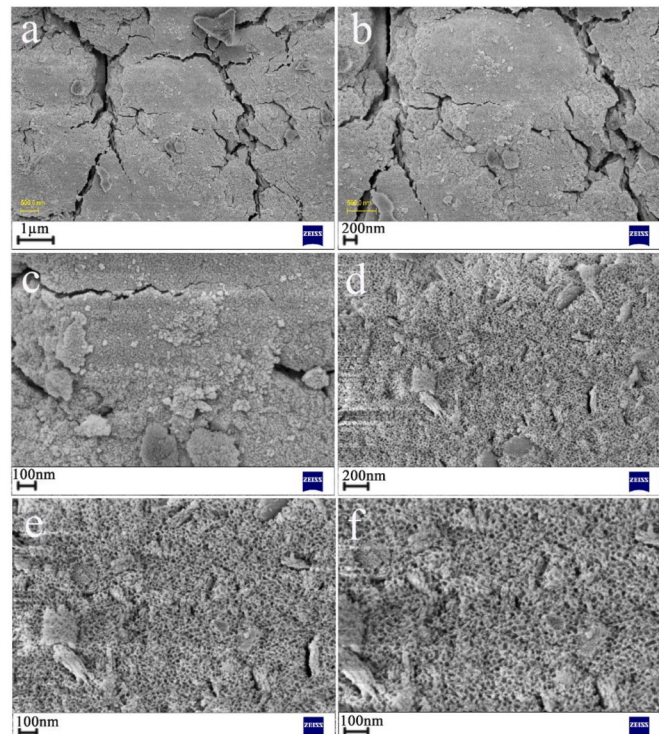


**Fig. 2.** FE-SEM analysis of CeO<sub>2</sub> NPs after 20 min (a–c) and after 5 min of sonication (d–f).

and c), the  $\text{CeO}_2$  particles appear to have clear boundaries and are less clustered, indicating that extended sonication times may encourage individual particle growth over collective nucleation. Contrastingly, the SEM images d-f, associated with a 5-min sonication duration, reveal a markedly different scenario—a densely populated nanoparticulate field where the  $\text{CeO}_2$  NPs are in closer proximity, displaying minimal growth and aggregation. The high-density packing observed in image d (1  $\mu\text{m}$  scale) suggests a rapid nucleation process that is curtailed before significant particle growth can occur.

Further magnified views at 200 nm and 100 nm (images e and f) show a tightly bound nanoparticle network, indicative of a synthesis regime that favors the formation of nanoparticles with a high surface area relative to volume. Such characteristics are particularly advantageous for catalytic processes, as they provide a greater active site density for interactions with target pollutants.

The SEM analysis corroborates the hypothesis that a 5-min sonication time is beneficial in producing a nanoparticulate matrix that is less agglomerated and finely dispersed, with an average particle size of approximately 20 nm. However, the suggestion to employ a 10-min sonication time as the optimum condition proposes an intermediate approach—potentially optimizing the balance between nucleation and particle growth, to yield  $\text{CeO}_2$  NPs with morphological characteristics tailored for enhanced reactivity in environmental applications.

The FE-SEM images in Fig. 3 vividly illustrate the impact of varying concentrations of glucose as a capping agent on the morphology of cerium oxide nanoparticles ( $\text{CeO}_2$  NPs). In the images a-c, where 2 mmol of glucose was utilized, the resulting nanoparticles are seen with substantial cracking and aggregation, suggesting that an excess of glucose might encourage particle growth and potential fusion. This is particularly evident in the image captured at a 1  $\mu\text{m}$  scale, which shows an uneven distribution of larger nanoparticles, and the phenomenon becomes even more pronounced at a scale of 200 nm. Upon closer inspection at a 100 nm scale, a high density of tightly clustered nanoparticles is observed, indicating that at this higher glucose concentration, the tendency towards agglomeration is pronounced.

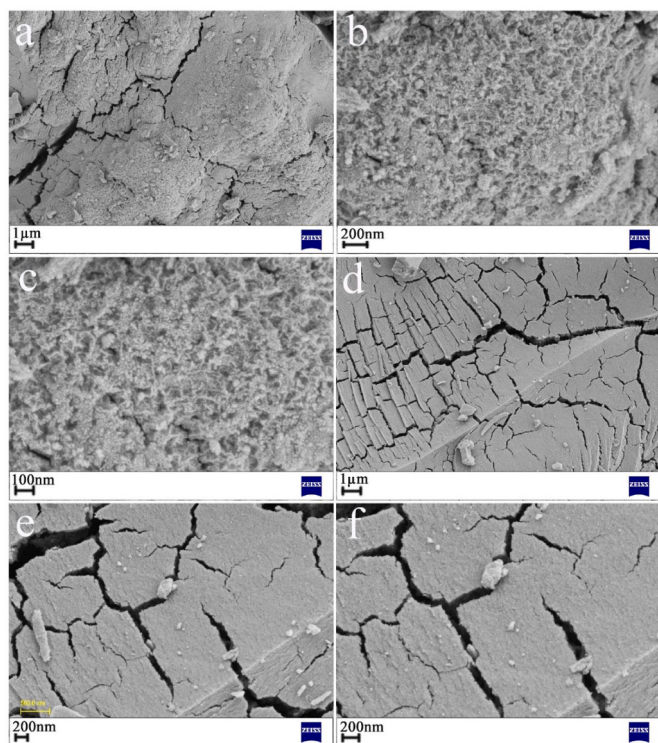


**Fig. 3.** FE-SEM images of  $\text{CeO}_2$  NPs after using 2 mmol glucose (a–c) and 0.5 mmol glucose (d–f).

In contrast, the images d-f, synthesized with a lower glucose concentration of 0.5 mmol, reveal a notably different nanoparticle landscape. The 1  $\mu\text{m}$  scale image presents a smoother and more uniform distribution of  $\text{CeO}_2$  NPs, with significantly fewer cracks, suggesting a more tempered synthesis process attributed to the reduced glucose content. Advancing to a 200 nm view, the benefits of lesser glucose are even more apparent; the nanoparticles exhibit a uniform dispersion with reduced clustering. The image at the same 200 nm scale further emphasizes this observation, showing a homogenous distribution of nanoparticles, indicative of a successful synthesis process that prevents excessive agglomeration, favoring the formation of nanoparticles with consistent sizes and shapes.

From these observations, it is inferred that a glucose concentration of 1 mmol, not visually represented in the provided images but mentioned as optimal, strikes a delicate balance between the overgrowth and excessive agglomeration seen with 2 mmol of glucose, and the under-developed morphology resulting from 0.5 mmol of glucose. Thus, the tuning of glucose concentration is crucial for achieving the desired nanoparticle size and morphology, with implications for the efficacy of  $\text{CeO}_2$  NPs in catalytic and environmental applications [33].

FE-SEM images in Fig. 4 from further investigation into reaction parameters offer insight into the morphological changes of  $\text{CeO}_2$  nanoparticles under varying synthesis conditions. In the absence of ultrasonic waves (sample 8), the images a-c depict bulk structures with extensive cracking and agglomeration, highlighting the essential role of sonication in achieving smaller particle sizes. Without the use of a capping agent (sample 9), as shown in images d-f, nanoparticles exhibit irregular shapes and a broad size distribution, indicating the capping agent's importance in ensuring uniformity.

Despite this irregularity, the nanoscale nature of the particles in sample 9 provided a suitable blank for subsequent comparative analyses. This sample was utilized to benchmark the catalytic properties and performance against sample 5, which had been synthesized with glucose as a capping agent. This comparison aimed to isolate and understand the specific impact of the glucose capping agent on the catalytic efficiency and other relevant properties of the  $\text{CeO}_2$  nanoparticles.

Substituting  $\text{NH}_3$  with  $\text{NaOH}$  as the reducing agent (sample 10) results in densely packed agglomerates with poorly defined particles, as evidenced by images g-i. These comparative analyses confirm that the synthesis parameters optimized for sample 5 are critical for producing  $\text{CeO}_2$  nanoparticles with desired morphological characteristics, reaffirming its status as the optimal sample. Generally, for non-optimal conditions, the nanoparticles tend to agglomerate more significantly, potentially leading to the film-like appearance observed in some SEM images.

During the sonication-assisted synthesis of  $\text{CeO}_2$  nanoparticles, several chemical reactions take place involving the precursor and the reactive species generated by the ultrasonic waves. During the sonication process, a multitude of reactive species are generated, which contribute to the synthesis and surface modification of nanoparticles. The collapse of cavitation bubbles produces localized high temperatures and pressures, leading to the dissociation of water molecules and the generation of a range of reactive species. The primary species formed during sonication include hydroxyl radicals ( $\cdot\text{OH}$ ), hydrogen atoms ( $\text{H}^\bullet$ ), and hydrated electrons ( $\text{e}^- (\text{aq})$ ). These reactive species can contribute to the reduction of cerium ions and influence the formation and growth of cerium oxide nanoparticles [34,35].

In the case of cerium oxide nanoparticle synthesis, the hydroxyl radicals can react with cerium ions to form cerium hydroxides, which upon calcination, transform into the oxide form. The hydrogen atoms and hydrated electrons may further reduce cerium ions, influencing the  $\text{Ce(III)}$  to  $\text{Ce(IV)}$  ratio in the nanoparticles. These reactive species can also initiate the formation of additional oxygen vacancies and defects on the nanoparticle surface, which are critical for catalytic activity. Additionally, superoxide radicals ( $\text{O}_2^\cdot$ ) can be produced through the reaction of molecular oxygen dissolved in the solvent with the hydrated

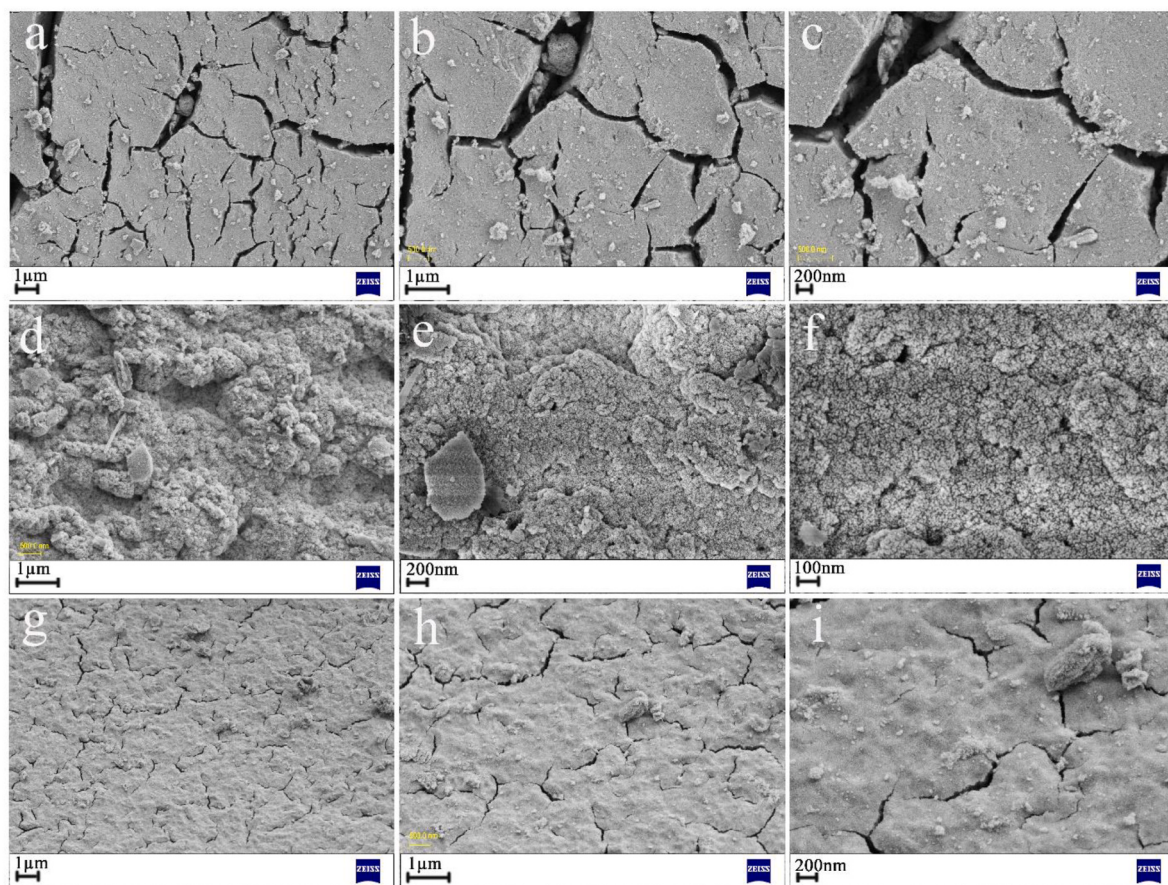


**Fig. 4.** FE-SEM of  $\text{CeO}_2$  NPs for sample 8 (a–c), sample 9 (d–f) and sample 10 (g–i).

electrons. These superoxide radicals can participate in oxidation reactions or recombine to form hydrogen peroxide ( $\text{H}_2\text{O}_2$ ), which can further dissociate into hydroxyl radicals [36].

### 3.2. Elemental and structural analysis

Following the scrutiny of SEM images that identified sample 5 as the optimum sample, additional characterizations were performed to understand its composition and structure in detail. The Energy-Dispersive X-ray Spectroscopy (EDS) analysis, complemented by the elemental mapping images, provides a detailed insight into the composition and distribution of elements in the  $\text{CeO}_2$  nanoparticles characterized in sample 5 (Fig. 5). The EDS spectrum reveals the presence of distinctive peaks for cerium (Ce) and oxygen (O), establishing the material's identity as  $\text{CeO}_2$ . Atomic percentage data from the EDS quantification shows oxygen at approximately 76.62 % and cerium at 23.38 %, a ratio that slightly exceeds the expected stoichiometric ratio for  $\text{CeO}_2$  but could be indicative of surface-adsorbed oxygen rather than a fundamental compositional imbalance.

The morphological SEM image exhibits well-defined grain boundaries and a cracked structure typical of nanoparticles post-synthesis, indicating a crystalline formation with the characteristic drying patterns. The elemental maps, displayed in a composite overlay and individually for cerium and oxygen, portray a homogeneous elemental distribution. Cerium's presence, shown in green, is densely spread across the nanoparticles, and the oxygen distribution, depicted in red, mirrors this uniformity. The consistency in the intensity of the colors across the maps indicates an even distribution of both cerium and oxygen, confirming a uniform chemical composition throughout the sample.

The X-Ray Diffraction (XRD) patterns of samples 5 and 9, with sample 9 serving as the blank, reveal distinct crystalline characteristics

of the cerium oxide nanoparticles synthesized in sample 5 (Fig. 6). The XRD patterns matched the JCPDS card number 00-034-0394, confirming the phase and crystallinity of the synthesized  $\text{CeO}_2$  [37]. The sharp and well-defined peaks in the XRD pattern of sample 5 correspond to the fluorite structure of crystalline  $\text{CeO}_2$ , indicating a high degree of crystallinity and purity in the synthesized nanoparticles. In contrast, the XRD pattern of the blank sample 9 displays diffuse and poorly defined peaks, suggesting a lack of crystalline structure and confirming the amorphous nature of the blank. This stark difference substantiates the effectiveness of the synthesis process for sample 5, culminating in nanoparticles that exhibit the crystalline attributes necessary for enhanced catalytic activity and stability, as compared to the non-crystalline blank.

On the other hand, the crystallite size of  $\text{CeO}_2$  nanoparticles, determined using the Scherrer equation from the XRD data, was 5.95 nm for the optimized sample 5 and 11.91 nm for the blank sample 9. The smaller size in sample 5 suggests a controlled synthesis process, enhancing the nanoparticles' surface area and potential catalytic properties, whereas the larger size in sample 9 indicates a less regulated crystallite formation [38].

The Diffuse Reflectance Spectroscopy (DRS) analysis and the obtained Tauc plot for samples 5 and 9 reveal distinct optical properties of the  $\text{CeO}_2$  nanoparticles in Fig. 7. While our approach focuses on spectroscopy and the resulting Tauc plot, some researchers have successfully applied machine learning techniques to predict the band gaps of a wide array of materials, suggesting a complementary pathway for future enhancements in prediction accuracy [39]. Sample 5, with a band gap of 2.5 eV, exhibits a sharp absorption edge in the UV region, suggesting a strong potential for photocatalytic applications under UV and possibly visible light. The corresponding Tauc plot confirms a direct electronic transition, indicative of a material poised for effective light-energy

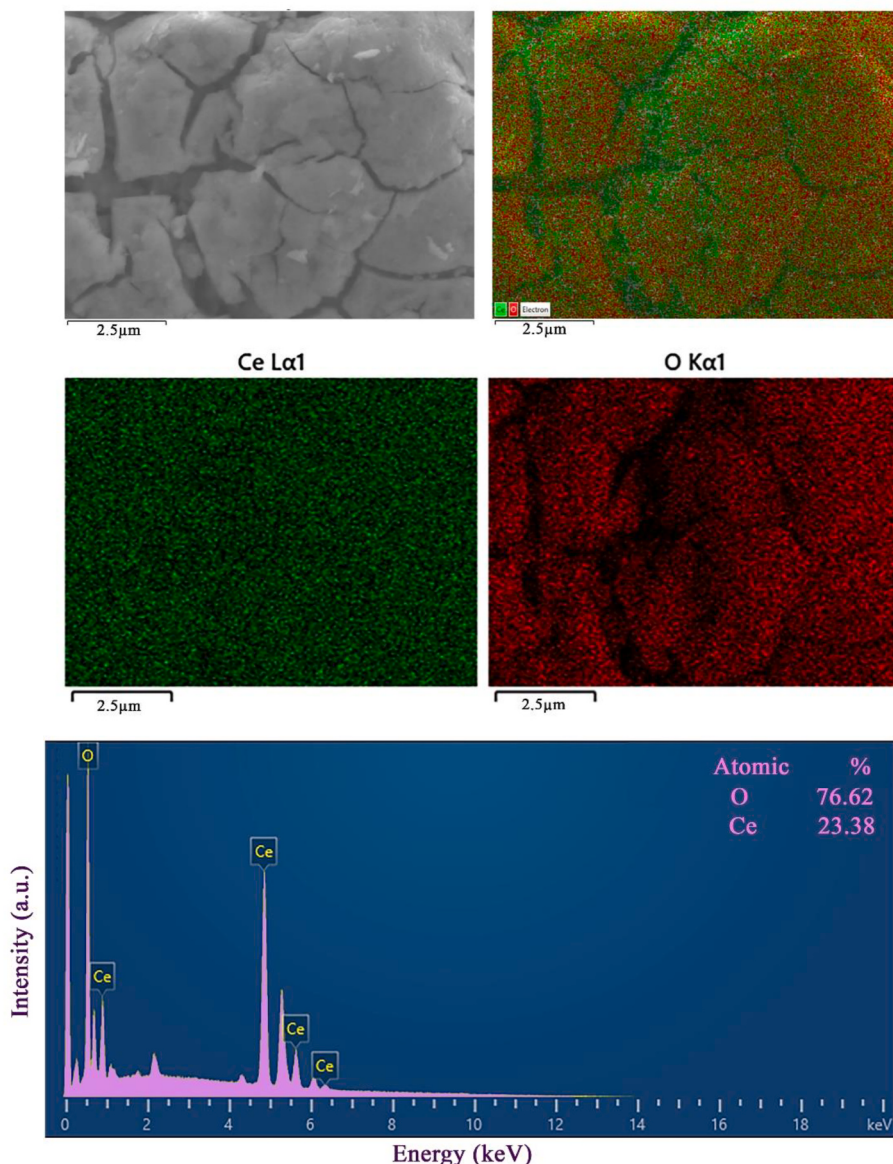


**Fig. 5.** EDS analysis and mapping images of  $\text{CeO}_2$  NPs obtained for sample 5.

utilization.

In contrast, sample 9 shows a slightly wider band gap of 2.66 eV, as evidenced by its DRS spectrum with a less sharp absorption edge, hinting at the influence of the absent capping agent on the nanoparticles' electronic structure. This larger band gap could restrict the photocatalytic activity to a narrower UV range [40].

Brunauer-Emmett-Teller (BET) and Barrett-Joyner-Halenda (BJH) analyses were conducted to evaluate the surface properties of  $\text{CeO}_2$  nanoparticles in samples 5 and 9 (Fig. 8).

The results for sample 5 revealed a high surface area of  $102.27 \text{ m}^2/\text{g}$  and a pore volume of  $0.06676 \text{ cm}^3/\text{g}$  with pores averaging  $2.6112 \text{ nm}$  in diameter, suggesting a uniform distribution of mesopores. Such uniformity is crucial for consistent photocatalytic activity as it ensures more predictable diffusion paths for reactants, facilitating effective interactions with the catalyst's active sites. Conversely, the BJH pore size distribution for Sample 9 is broader with a less distinct peak, indicating a more varied pore size distribution [41]. Also, sample 9 displayed a lower surface area of  $72.9 \text{ m}^2/\text{g}$ , a pore volume of  $0.06397 \text{ cm}^3/\text{g}$ , and a larger pore diameter of  $3.51 \text{ nm}$ . The increased pore size and reduced surface area in sample 9, lacking a glucose capping agent, may lead to

diminished catalytic efficiency. These findings underscore the significant role of synthesis modifications, particularly the inclusion of a capping agent, in enhancing the textural characteristics essential for photocatalytic applications of  $\text{CeO}_2$  nanoparticles. A summary of this data can be found in Table 2.

The nitrogen adsorption-desorption isotherms for both Sample 5 and Sample 9 are classified as type IV according to IUPAC standards, indicative of mesoporous materials. This classification is supported by the presence of a capillary condensation step observed within a middle range of relative pressures, typical of mesopores. Both samples exhibit hysteresis loops, which further affirm the mesoporous nature of the materials. The hysteresis loop observed in Sample 5 corresponds to type H3, commonly associated with slit-shaped pores that result from the aggregation of plate-like particles [42]. This loop type suggests non-uniform and irregular pores, characteristic of dynamically synthesized particles under sonochemical conditions [43]. For Sample 9, the type H3 hysteresis loop is also present but is less pronounced, implying a presence of larger, more irregularly shaped pores compared to Sample 5.

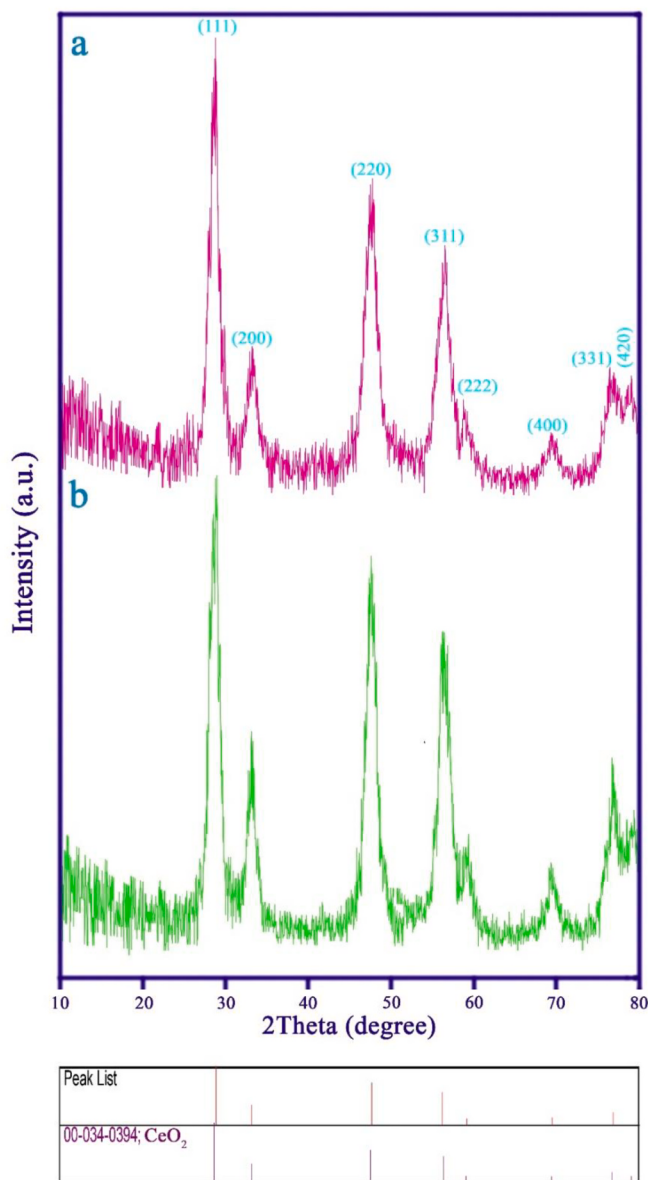


**Fig. 6.** XRD pattern for CeO<sub>2</sub> NPs obtained for samples 5 (a) and sample 9 (b).

### 3.3. Investigations into contaminant decomposition

The photocatalytic activities of the synthesized CeO<sub>2</sub> nanostructures were assessed by examining their effectiveness in degrading various contaminants in an aqueous medium under visible light exposure from a 125 W Osram lamp. For each assay, 48 mg of the nanocatalyst was dispersed into 50 ml of a solution containing 1.2 mg of the target contaminant. This suspension was stirred in darkness for 30 min to establish an adsorption-desorption equilibrium before the illumination was initiated. The degradation rate of the toxic contaminants was determined by calculating the ratio  $(A_t/A_0) \times 100$ . Subsequently, the rate of degradation as a function of illumination time was graphically represented to evaluate the nanocatalysts' performance [34]. Fig. 9 delineates the photocatalytic degradation of Acid red 14 using synthesized nanocatalysts from samples 5, 8, and 9 under visible light, with TiO<sub>2</sub> nanoparticles (P25) for comparative analysis and a catalyst-free sample as a control sample without any catalyst to account for self-degradation. The results reveal that sample 5 significantly outperforms the rest, achieving an impressive 97.2 % degradation efficiency, highlighting its superior photocatalytic activity.

Sample 9, devoid of a glucose capping agent, shows commendable activity with an 83.71 % reduction, while sample 8, synthesized without ultrasonic waves, lags behind at 38.21 %. Notably, the commercial TiO<sub>2</sub> (P25) nanoparticles exhibit a lower degradation efficiency of 9.7 %, unexpectedly underperforming against the synthesized samples. These observations underscore the efficacy of the synthesis process for sample 5, particularly the role of glucose as a capping agent in enhancing photocatalytic performance, and affirm the critical influence of specific synthesis conditions on the functionality of CeO<sub>2</sub> nanoparticles.

Fig. 10 showcases the application of the Langmuir-Hinshelwood kinetic model to describe the pseudo-first-order kinetics for the photocatalytic degradation of Acid Red 14 by various nanocatalysts, including commercial TiO<sub>2</sub> (P25) and sonochemically prepared samples 5, 8, and 9. The model, expressed as  $\ln(C/C_0) = -kt$ , where  $C_0$  is the initial concentration of the contaminant,  $C$  is the concentration at time  $t$ , and  $k$  is the rate constant, is commonly used to analyze the photocatalytic activity.

The logarithmic concentration ratio,  $\ln(C/C_0)$ , plotted against time, demonstrates that sample 5 exhibits the most rapid degradation, as evidenced by the steepest slope and highest rate constant of  $0.0701 \text{ min}^{-1}$ . This superior performance is significantly greater than that of sample 9 ( $k = 0.0096 \text{ min}^{-1}$ ), sample 8 ( $k = 0.0382 \text{ min}^{-1}$ ), and notably surpasses the commercial TiO<sub>2</sub>, which has the lowest rate constant of  $0.0021 \text{ min}^{-1}$ . The comparison graph unequivocally establishes sample 5 as the most efficient photocatalyst among those tested, highlighting the effectiveness of the sonochemical synthesis process in optimizing the photocatalytic activity of CeO<sub>2</sub> nanoparticles.

Fig. 11 illustrates the impact of varying doses of CeO<sub>2</sub> nanoparticles from sample 5 and different concentrations of Acid Red 14 on the degradation efficiency. The results indicate that an increase in the nanoparticle dosage leads to higher degradation percentages, with the efficiency climbing from 74.1 % at the lowest dosage to a peak of 97.2 % at the highest dosage. This suggests that greater quantities of the nanocatalyst enhance the photocatalytic reaction by providing more active sites. Conversely, the degradation efficiency inversely correlates with the concentration of Acid Red 14; higher dye concentrations decrease the degradation percentage to as low as 62.8 %, while lower concentrations facilitate a more efficient degradation, achieving up to 97.2 %. These findings highlight the significance of nanoparticle dosage and contaminant concentration in optimizing the photocatalytic degradation capabilities of CeO<sub>2</sub> nanoparticles from sample 5.

These findings illustrate the nuanced interplay between catalyst dosage and contaminant concentration, with 50 mg of CeO<sub>2</sub> nanoparticles emerging as the optimal amount for the photocatalytic degradation of Acid Red 14, ensuring maximal degradation performance.

Fig. 12 provides a clear visualization of scavenging experiments aimed at identifying the main active species responsible for the photocatalytic degradation of a contaminant by sample 5. With no scavenger present, sample 5 achieves a 97.2 % degradation rate, indicating its high intrinsic photocatalytic activity. When isopropyl alcohol (IPA), a known •OH scavenger, is introduced, the degradation rate dramatically decreases to 28.7 %. This significant reduction suggests that hydroxyl radicals are a primary active species in the photocatalytic process of sample 5. The addition of Vitamin C (VIT C), which is an effective scavenger of h<sup>+</sup> (holes), results in a degradation rate of 48.6 %. This indicates that electron vacancies also play a crucial role in the photocatalytic reaction, albeit not as dominantly as the hydroxyl radicals. The presence of potassium iodide (KI), which scavenges •O<sub>2</sub><sup>-</sup> (superoxide radicals), shows a lesser impact on the photocatalytic activity, with a degradation rate of 80.9 %. This suggests that superoxide radicals do contribute to the photocatalysis but are not the primary reactive species [44,45].

The results from these scavenging experiments reveal that hydroxyl radicals and holes are the predominant oxidative agents driving the photocatalytic degradation in sample 5. The hydroxyl radicals, in particular, are the most influential, considering the substantial decrease

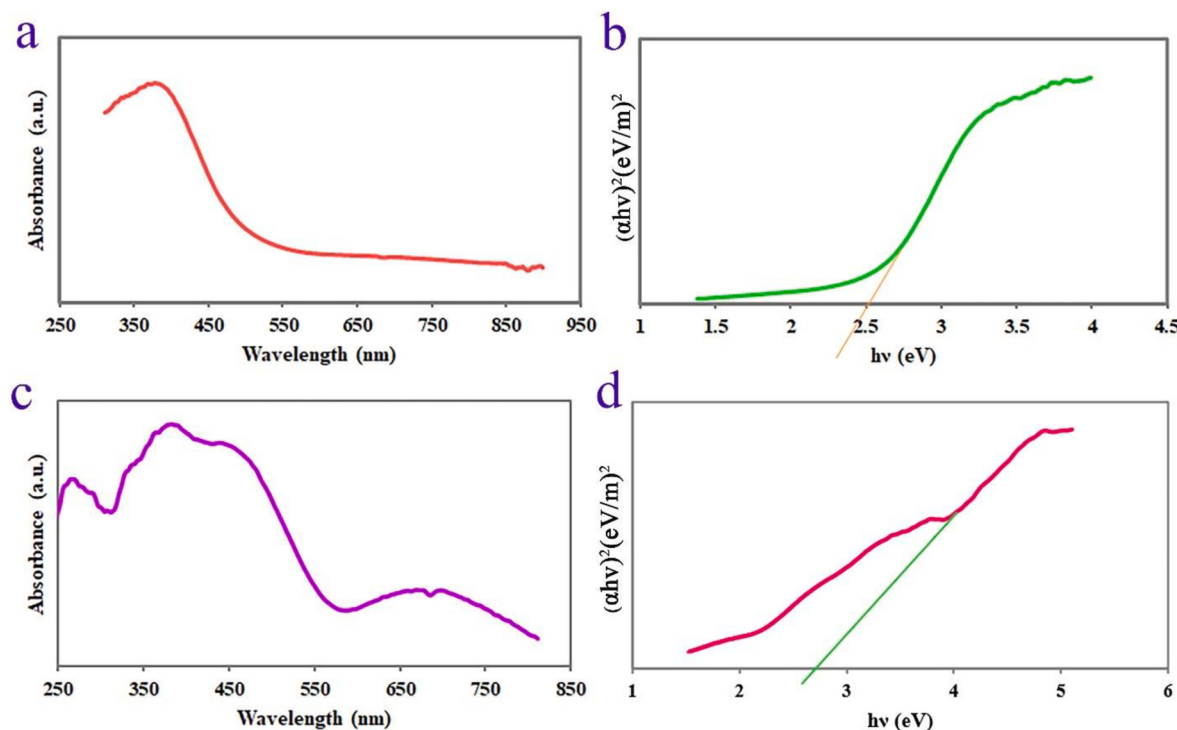


Fig. 7. DRS and Tauc plots of sample 5 (a, b) and sample 9 (c, d).

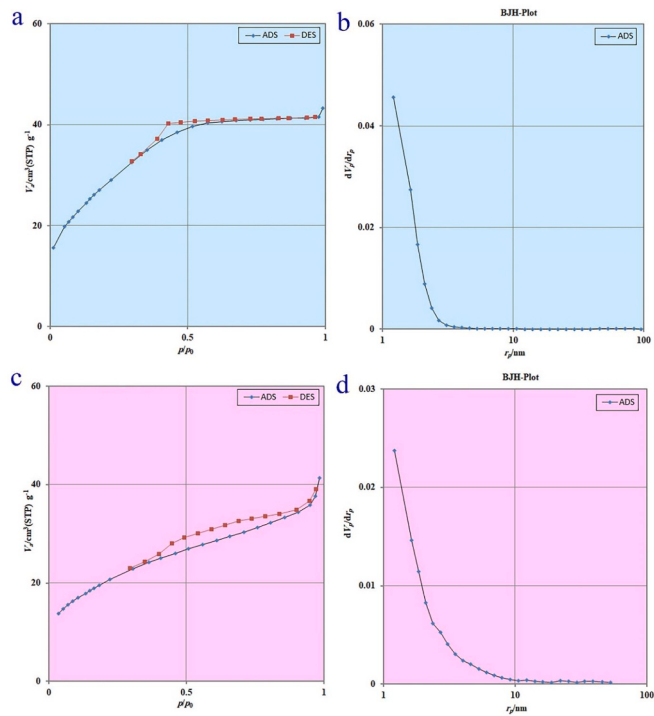


Fig. 8. BET-BJH results for sample 5 and sample 9.

**Table 2**  
Summary of BET-BJH results for sample 5 and sample 9.

Photocatalyst	BET area ( $\text{m}^2 \text{ g}^{-1}$ )	Pore volume ( $\text{cm}^3 \text{ g}^{-1}$ )	Pore diameter (nm)
Sample 5	102.27	0.06676	2.6112
Sample 9	72.9	0.06397	3.51

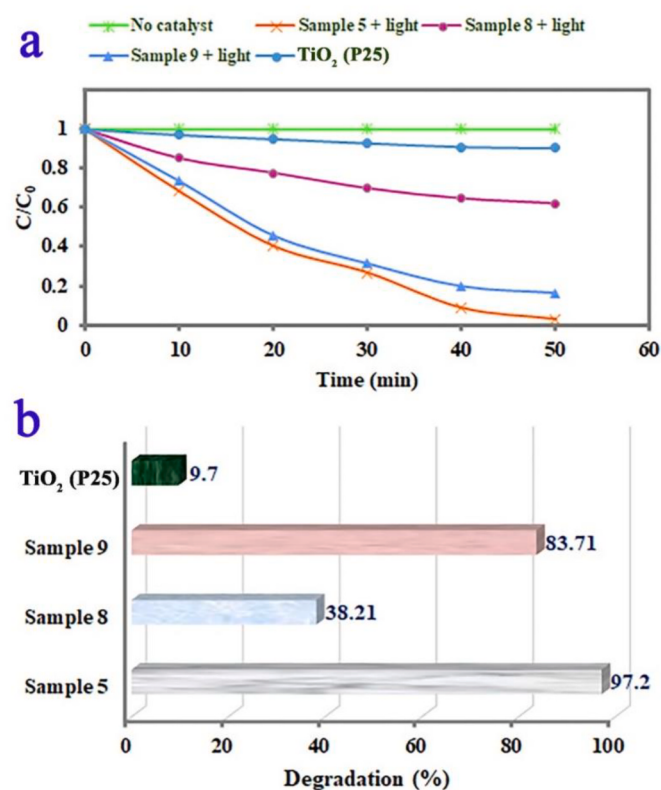
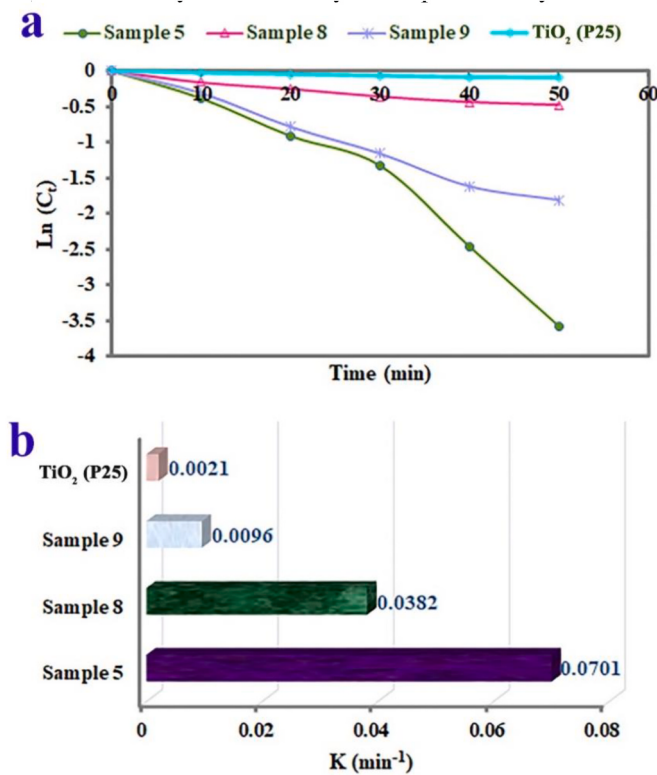


Fig. 9. (a) The photocatalytic activities of as-synthesized nanocatalyst and (b) comparison of photocatalytic efficiency.



**Fig. 10.** The Langmuir Hinshelwood model for photocatalytic decomposition of acid red 14 in the presence of commercial  $\text{TiO}_2$ , Sample 5, 8 and 9. (For interpretation of the references to color in this figure legend, the reader is referred to the Web version of this article.)

in degradation observed when they are scavenged.

### 3.4. Stability and reusability assessment

The reusability of sample 5 nanocatalyst is depicted in Fig. 13a, where the catalyst, at a consistent weight of 50 mg, is used to treat a 50 mL dye solution containing Acid Red 14 with a concentration of 1.2 mg, subjected to visible light for a duration of 50 min, across 11 consecutive cycles. The initial cycle shows a high degradation rate of 97.2 %, which experiences a gradual decrease to 87.8 % by the 11th cycle.

This trend suggests a slow decline in the nanocatalyst's effectiveness, which could be due to the saturation of the catalyst's active sites by the dye or its degradation byproducts, a slight loss of the catalytic material through the repeated reuse, or alterations to the nanocatalyst's characteristics over the course of the treatment cycles. Despite this, the catalyst retains a notable degree of activity over numerous cycles, highlighting its durability and potential for repetitive use.

The XRD pattern presented in Fig. 13b for sample 5 after undergoing 11 photocatalytic cycles can be compared to the initial XRD pattern provided earlier to assess any changes in the crystalline structure of the nanocatalyst. The pattern in Fig. 13b shows sharp peaks corresponding to the characteristic crystal planes of cerium oxide, indicating that the crystalline structure is well-preserved even after multiple cycles of photocatalytic activity. The maintenance of peak positions and intensities when compared to the initial XRD pattern suggests that the crystallinity of the catalyst has not been compromised through reuse. There are no new peaks or noticeable peak broadening, which would indicate structural changes or a decrease in crystallite size. The enduring crystalline integrity as evidenced by the XRD analysis is a likely contributor to the stability and reusability of the photocatalyst. It suggests that the catalytic material does not undergo significant structural degradation or loss of crystallinity, which could otherwise lead to a

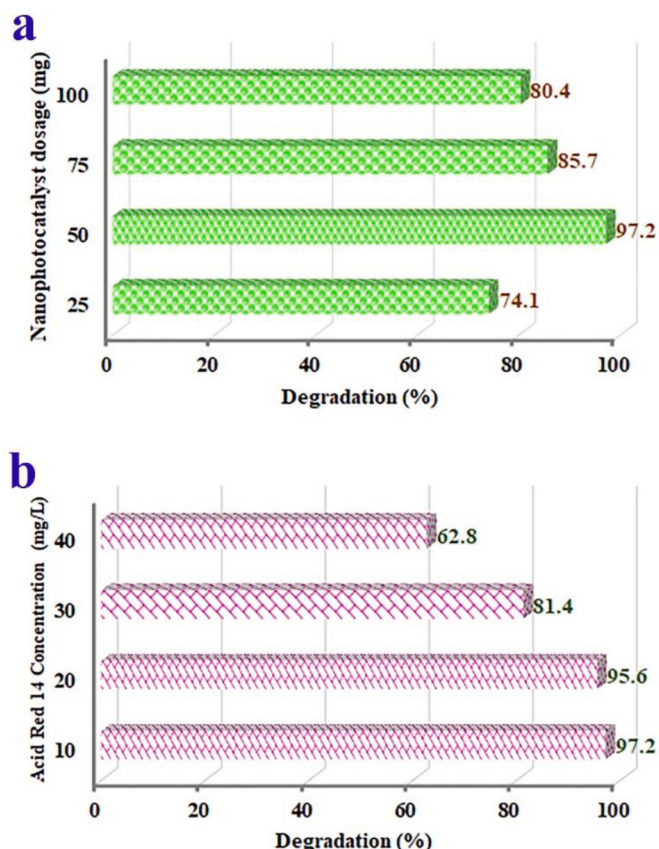


**Fig. 11.** Influence of (a) dosing of  $\text{CeO}_2$  nanoparticles and (b) Acid Red 14 concentration on degradation efficacy. (For interpretation of the references to color in this figure legend, the reader is referred to the Web version of this article.)

decline in photocatalytic performance.

Our exploration of the mechanism governing the photocatalytic decomposition of Acid Red 14 by cerium oxide nanoparticles, initiates with an investigation into the nanoparticles' responsiveness to visible light, leading to the subsequent formation of reactive species (Schematic 2). The following is a proposed mechanism for the photocatalytic degradation of Acid Red 14 by  $\text{CeO}_2$  nanoparticles synthesized with the assistance of ultrasonic waves and glucose as a capping agent [46,47]:

1. Generation of reactive species on  $\text{CeO}_2$  surface:
  - Under visible light irradiation, the  $\text{CeO}_2$  nanoparticles become excited, promoting electrons ( $e^-$ ) from the valence band to the conduction band and leaving behind holes ( $h^+$ ) in the valence band.
  - The presence of oxygen vacancies in  $\text{CeO}_2$ , which are characteristic features enhanced by the sonication process, can trap the photo-generated electrons, thereby prolonging the lifetime of the reactive species.
2. Formation of Radicals:
  - The holes ( $h^+$ ) in the valence band can oxidize water molecules or hydroxide ions to form hydroxyl radicals ( $\cdot\text{OH}$ ).
  - The trapped electrons ( $e^-$ ) at the oxygen vacancy sites can reduce molecular oxygen ( $\text{O}_2$ ) adsorbed on the nanoparticle surface to superoxide radicals ( $\cdot\text{O}_2^-$ ).
3. Degradation of Acid Red 14:
  - The hydroxyl radicals ( $\cdot\text{OH}$ ), known for their strong oxidative potential, can attack the dye molecules, leading to the breakdown of chromophores and the cleavage of complex organic structures.

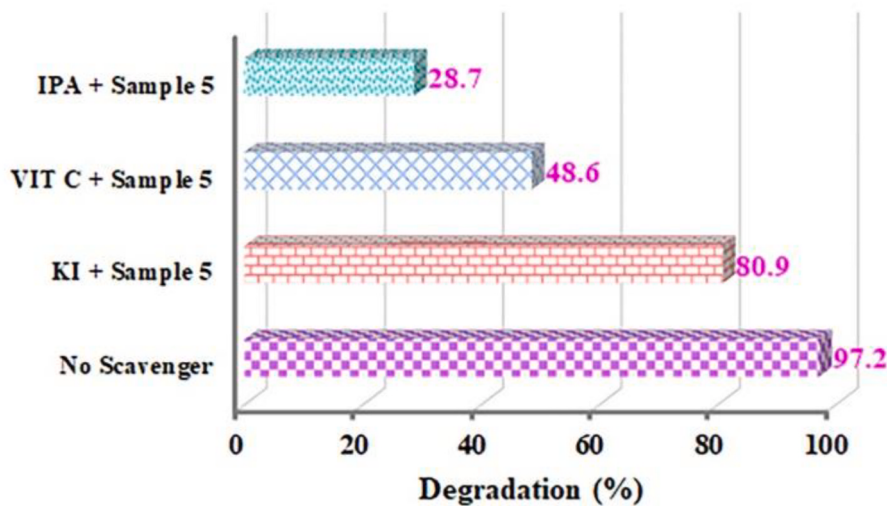


**Fig. 12.** Scavenger tests in presence of isopropyl alcohol (IPA), Vitamin C (VIT C) and potassium iodide (KI) suppressors.

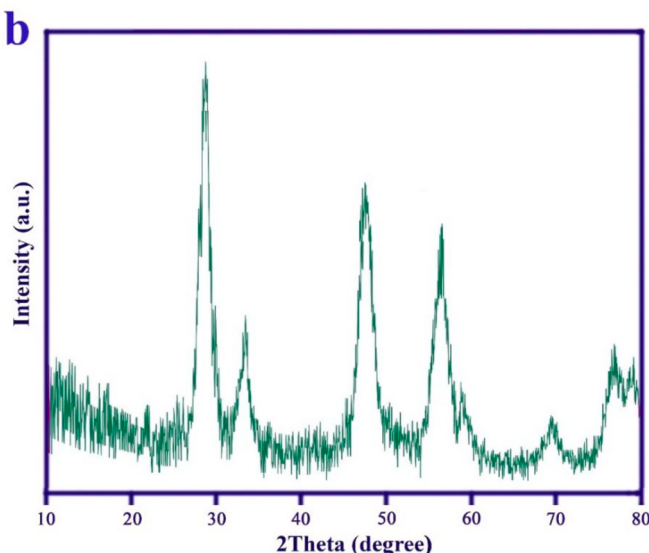
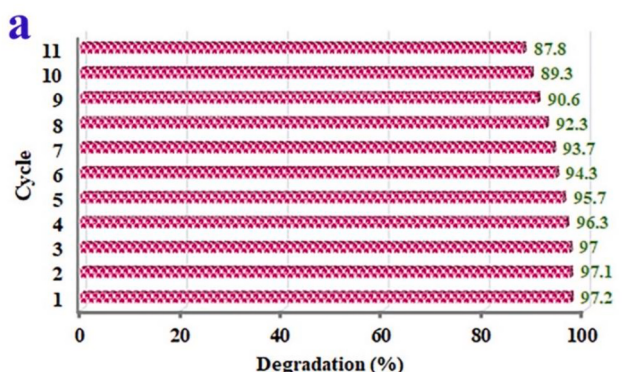


**Fig. 13.** (a) The recyclability experiment for sample 5 and (b) its XRD pattern after undergoing 11 photocatalytic cycles.

- The superoxide radicals  $\cdot(\text{O}_2^-)$  can initiate further oxidation reactions or dismutate to hydrogen peroxide ( $\text{H}_2\text{O}_2$ ), which can also decompose to form more hydroxyl radicals.
- Holes ( $\text{h}^+$ ) can directly oxidize the dye molecules, contributing to the degradation process.

#### 4. Reactions Leading to Mineralization:

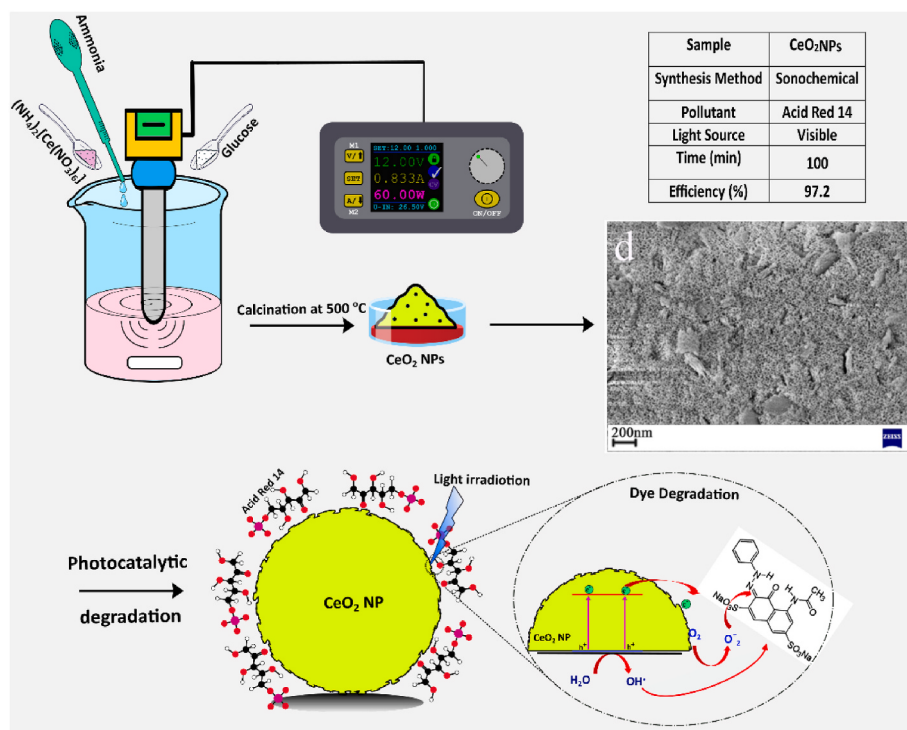
- The continuous attack by the reactive species leads to the degradation of Acid Red 14 into smaller intermediates, which are further broken down into mineral acids,  $\text{CO}_2$ ,  $\text{H}_2\text{O}$ , and other less harmful or non-harmful end products.

**Fig. 14** illustrates the photocatalytic degradation prowess of sample 5, which demonstrates exceptional efficiency in the breakdown of various pollutants under visible light conditions. The nanocatalyst exhibits a remarkable degradation efficiency of 97.2 % for Acid Red 14, 98.7 % for Malachite Green, an impressive 99.1 % for Captopril, and 98.3 % for Amlodipine, showcasing its robust performance across a diverse range of contaminants. The UV-Vis spectral data corroborates these findings, with significant reductions in absorbance peaks signifying the effective dismantling of the pollutants' molecular structures within a 50-min irradiation period. The consistently high degradation percentages for all tested pollutants underscore the versatility and efficacy of sample 5 as a photocatalyst, marking its potential for widespread application in the purification of contaminated water.

**Table 3** presents a comprehensive analysis of the photocatalytic efficiencies of various cerium oxide ( $\text{CeO}_2$ ) nanoparticles synthesized through different methods, illustrating the enhanced performance of our sonochemically synthesized nanoparticles. With a degradation efficiency of 97.2 % against Acid Red 14 under visible light, our nanoparticles not only demonstrate superior activity but also do so within a relatively short reaction time of 100 min. This marks a significant improvement over nanoparticles produced by traditional hydrothermal methods, which only achieve a 74.04 % efficiency against Methylene Blue under sunlight.

Our results are particularly compelling when compared to doped or composite nanostructures such as  $\text{CeO}_2\text{-TiO}_2$  nanocomposites and Zn-doped  $\text{CeO}_2$  NPs. These systems, while effective, often require UV light and longer exposure times to reach high efficiencies. For example,  $\text{CeO}_2\text{-TiO}_2$  nanocomposites, though achieving a high degradation efficiency of 95 %, necessitate 150 min and the presence of UV and visible light, highlighting the time-efficiency and simpler light requirements of our nanoparticles.

Moreover, the broad-spectrum activity of our sonochemically synthesized nanoparticles against various pollutants underscores their versatility and contrasts with other nanostructures that often exhibit selective efficiency. Notably, our nanoparticles outperform  $\text{CeO}_2$  nanowires and  $\text{CeO}_2/\text{Bi}_2\text{WO}_6$  composites, which show lower efficiencies and require specific conditions such as different light sources and longer reaction times.



Sch. 2. The photocatalytic mechanism of CeO<sub>2</sub> NPs and the significant outcomes.

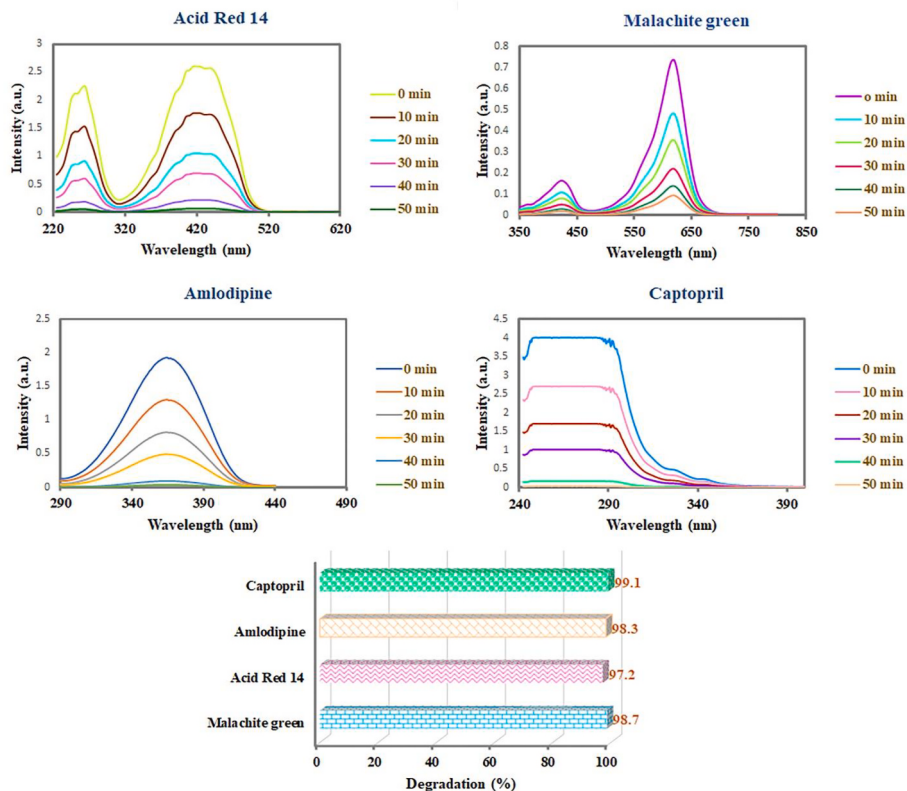


Fig. 14. UV-vis absorption spectra depicting the degradation performance of sample 5 nanocatalyst, against various pollutants under visible light irradiation.

The superior efficiency, shorter reaction time, and ability to operate effectively under visible light without the necessity for UV radiation make our sonochemically synthesized CeO<sub>2</sub> nanoparticles particularly attractive for practical applications in environmental remediation. Their

high degradation efficiency across a range of pollutants also highlights their potential to address diverse environmental challenges, providing a versatile and efficient solution for the degradation of complex organic pollutants in water systems.

**Table 3**Comparison of CeO<sub>2</sub> NPs synthesized in this research with other CeO<sub>2</sub> nanostructures.

Sample	Synthesis Method	Pollutant	Light Source	Time (min)	Efficiency (%)	Reference
CeO <sub>2</sub> NPs	Hydrothermal	Methylene Blue	Sunlight	30	74.04	[37]
CeO <sub>2</sub> –TiO <sub>2</sub> Nanocomposite	Green synthesis	Methylene Blue	UV & Vis	150	95	[48]
CeO <sub>2</sub> /Chitosan	Pechini method	Congo Red	UV	90	86.2	[46]
CeO <sub>2</sub> Nanowires	Hydrothermal	Methyl orange	UV	100	78	[49]
CeO <sub>2</sub> /Bi <sub>2</sub> WO <sub>6</sub>	Precipitation	RhB	Vis	120	44.4	[50]
Zn-doped CeO <sub>2</sub> NPs	Green synthesis	Acid Orange 7	Vis	180	83	[51]
CeO <sub>2</sub> NPs	Sonochemical	Acid Red 14	Vis	100	97.2	This research

#### 4. Conclusions

In this study, we have introduced a novel sonochemical method for synthesizing cerium oxide (CeO<sub>2</sub>) nanoparticles using glucose as a capping agent, significantly enhancing their photocatalytic properties under visible light. The optimal formulation achieved an impressive 97.2 % degradation efficiency for Acid Red 14, compared to only 9.7 % degradation using commercial TiO<sub>2</sub>. Moreover, the kinetics analysis revealed a rate constant of 0.0701 min<sup>-1</sup> for the optimized nanoparticles, markedly higher than that observed for other catalysts, demonstrating the efficacy of our approach.

The application of glucose as a capping agent effectively controlled the nanoparticle morphology and size distribution, which was instrumental in preventing agglomeration and enhancing stability. The resultant nanoparticles exhibited remarkable photocatalytic activity not only against Acid Red 14 but also against other contaminants like Amlodipine and Malachite Green, achieving degradation efficiencies of 98.3 % and 98.7 % respectively. Furthermore, the synthesized nanoparticles maintained their catalytic performance over multiple cycles, with a minimal decrease in activity, from 97.2 % in the first cycle to 87.8 % after 11 cycles, underscoring their durability and reusability.

#### Availability of data and material

Not applicable.

#### CRediT authorship contribution statement

**Sahar Zinatloo-Ajabshir:** Writing – review & editing, Writing – original draft, Visualization, Validation, Project administration, Methodology, Investigation, Funding acquisition, Data curation, Conceptualization. **Zohreh Mehrabadi:** Validation, Methodology, Investigation, Formal analysis, Data curation, Conceptualization. **Hossein Khojasteh:** Writing – original draft, Visualization, Validation, Investigation, Formal analysis, Data curation, Conceptualization. **Fariborz Sharifianjazi:** Resources, Investigation, Data curation, Conceptualization.

#### Declaration of competing interest

The authors declare that they have no known competing financial interests or personal relationships that could have appeared to influence the work reported in this paper.

#### Acknowledgement

Authors are grateful to the council of University of Bonab for supporting this work by Grant No (14013).

#### References

- [1] I. Bazhukova, I. Starostina, A. Myshkina, S. Bazhukov, I. Gavrilov, V. Meschaninov, CATALYTIC ACTIVITY OF CERIUM OXIDE NANOPARTICLES, 2020.
- [2] S.N. Naidi, M.H. Harunsani, A.L. Tan, M.M. Khan, Green-synthesized CeO<sub>2</sub> nanoparticles for photocatalytic, antimicrobial, antioxidant and cytotoxicity activities, *J. Mater. Chem. B* 9 (2021) 5599–5620.
- [3] K.R. Singh, V. Nayak, T. Sarkar, R.P. Singh, Cerium oxide nanoparticles: properties, biosynthesis and biomedical application, *RSC Adv.* 10 (2020) 27194–27214.
- [4] C. Walkey, S. Das, S. Seal, J. Erlichman, K. Heckman, L. Ghibelli, E. Traversa, J. F. McGinnis, W.T. Self, Catalytic properties and biomedical applications of cerium oxide nanoparticles, *Environ. Sci.: Nano* 2 (2015) 33–53.
- [5] A. Younis, D. Chu, S. Li, Cerium oxide nanostructures and their applications, *Funct. Nanomat* 3 (2016) 53–68.
- [6] E. Kusmirek, A CeO<sub>2</sub> semiconductor as a photocatalytic and photoelectrocatalytic material for the remediation of pollutants in industrial wastewater: a review, *Catalysts* 10 (2020) 1435.
- [7] T.V. Surendra, S.M. Roopan, Photocatalytic and antibacterial properties of phytosynthesized CeO<sub>2</sub> NPs using *Moringa oleifera* peel extract, *J. Photochem. Photobiol. B* 161 (2016) 122–128.
- [8] I. Celardo, E. Traversa, L. Ghibelli, Cerium oxide nanoparticles: a promise for applications in therapy, *J. Exp. Therapeut. Oncol.* 9 (2011) 47–51.
- [9] G. Casals, M. Perramón, E. Casals, I. Portolés, G. Fernández-Varo, M. Morales-Ruiz, V. Puntes, W. Jiménez, Cerium oxide nanoparticles: a new therapeutic tool in liver diseases, *Antioxidants* 10 (2021) 660.
- [10] H. Tang, H. E, C. Yao, X. Wang, J. Zhou, W. Song, Z. Zhang, Boosted antibiotic elimination over 2D/2D mesoporous CeO<sub>2</sub>/BiOCl S-scheme photocatalyst, *Separ. Purif. Technol.* 354 (2024) 128977.
- [11] Y. Zhu, C. Chen, P. Cheng, J. Ma, W. Yang, W. Yang, Y. Peng, Y. Huang, S. Zhang, G. Seong, Recent advances in hydrothermal synthesis of facet-controlled CeO<sub>2</sub>-based nanomaterials, *Dalton Trans.* 51 (2022) 6506–6518.
- [12] M. Panahi-Kalamuei, S. Alizadeh, M. Mousavi-Kamazani, M. Salavati-Niasari, Synthesis and characterization of CeO<sub>2</sub> nanoparticles via hydrothermal route, *J. Ind. Eng. Chem.* 21 (2015) 1301–1305.
- [13] F. Charbgoo, M.B. Ahmad, M. Darroudi, Cerium oxide nanoparticles: green synthesis and biological applications, *Int. J. Nanomed.* (2017) 1401–1413.
- [14] L. Yin, Y. Wang, G. Pang, Y. Koltypin, A. Gedanken, Sonochemical synthesis of cerium oxide nanoparticles—effect of additives and quantum size effect, *J. Colloid Interface Sci.* 246 (2002) 78–84.
- [15] S.A. Bukhari, H.A. Shakir, M. Khan, S. Saeed, I. Ahmad, M. Irfan, Biosynthesized cerium oxide nanoparticles CeO<sub>2</sub>NPs: recent progress and medical applications, *Curr. Pharmaceut. Biotechnol.* 24 (2023) 766–779.
- [16] J.T. Dahle, Y. Arai, Environmental geochemistry of cerium: applications and toxicology of cerium oxide nanoparticles, *Int. J. Environ. Res. Publ. Health* 12 (2015) 12523–1278.
- [17] W.-X. Tang, P.-X. Gao, Nanostructured cerium oxide: preparation, characterization, and application in energy and environmental catalysis, *Mrs Communications* 6 (2016) 311–329.
- [18] A.B. Shcherbakov, V.V. Reukov, A.V. Yakimansky, E.L. Krasnoperova, O.S. Ivanova, A.L. Popov, V.K. Ivanov, CeO<sub>2</sub> nanoparticle-containing polymers for biomedical applications: a review, *Polymers* 13 (2021) 924.
- [19] S. Patil, H.P. Dasari, Effect of fuel and solvent on soot oxidation activity of ceria nanoparticles synthesized by solution combustion method, *Mater.Sci. Energy Technol.* 2 (2019) 485–489.
- [20] M. Melchionna, P. Fornasiero, The role of ceria-based nanostructured materials in energy applications, *Mater. Today* 17 (2014) 349–357.
- [21] A. Dhall, W. Self, Cerium oxide nanoparticles: a brief review of their synthesis methods and biomedical applications, *Antioxidants* 7 (2018) 97.
- [22] H. Khojasteh, V. Mirkhani, M. Moghadam, S. Tangestaninejad, I. Mohammadpoor-Baltork, Palladium loaded on magnetic nanoparticles as efficient and recyclable catalyst for the suzuki- miyaura reaction, *J. NanoStruc.* 5 (2015) 271–280.
- [23] M.A. Salae, A. Salaeva, T.S. Kharlamova, G.V. Mamontov, Pt-CeO<sub>2</sub>-based composites in environmental catalysis: a review, *Appl. Catal. B Environ.* 295 (2021) 120286.
- [24] C.D. Walkey, J.B. Olsen, F. Song, R. Liu, H. Guo, D.W.H. Olsen, Y. Cohen, A. Emili, W.C. Chan, Protein corona fingerprinting predicts the cellular interaction of gold and silver nanoparticles, *ACS Nano* 8 (2014) 2439–2455.
- [25] A. Dhall, Cerium Oxide Nanoparticles: Their Phosphatase Activity and its Control, 2014.
- [26] D.-H. Lim, W.-D. Lee, D.-H. Choi, H.-H. Kwon, H.-I. Lee, The effect of cerium oxide nanoparticles on a Pt/C electrocatalyst synthesized by a continuous two-step process for low-temperature fuel cell, *Electrochim. Commun.* 10 (2008) 592–596.
- [27] D. Prieur, W. Bonani, K. Popa, O. Walter, K.W. Kriegsman, M.H. Engelhard, X. Guo, R. Eloirdi, T. Gouder, A. Beck, Size dependence of lattice parameter and electronic structure in CeO<sub>2</sub> nanoparticles, *Inorg. Chem.* 59 (2020) 5760–5767.
- [28] E.M. Ahmed, A.A. Alkathiri, Enhanced optical and electrical properties of CeO<sub>2</sub>NPs/chitosan nanocomposites, *Mater. Res. Express* 9 (2022) 055305.

- [29] K. Sudarshan, S. Sharma, R. Gupta, S.K. Gupta, F. Sayed, P. Pujari, Role of surface defects in catalytic properties of CeO<sub>2</sub> nanoparticles towards oxygen reduction reaction, *Mater. Chem. Phys.* 200 (2017) 99–106.
- [30] G. Spezzati, K. Fant, A. Ahniyaz, M. Lundin-Johnson, E.J. Hensen, H. Langermans, J.P. Hofmann, Synthesis, physicochemical characterization, and cytotoxicity assessment of CeO<sub>2</sub> nanoparticles with different morphologies, *Eur. J. Inorg. Chem.* 2017 (2017) 3184–3190.
- [31] S.N. Matussin, F. Khan, P. Chandika, M.H. Harunsani, N. Ahmad, Y.-M. Kim, W.-K. Jung, M.M. Khan,  $\alpha$ -Glucosidase inhibitory activity and cytotoxicity of CeO<sub>2</sub> nanoparticles fabricated using a mixture of different cerium precursors, *ACS Omega* 9 (2023) 157–165.
- [32] M. Hosseini, M. Haghghi, P. Margan, H. Ajamein, Comparative sonochemical synthesis of CeO<sub>2</sub>-doped Pd/clinoptilolite and Pd/Al<sub>2</sub>O<sub>3</sub> nanocatalysts used in total oxidation of toluene at low temperatures for polluted air treatment, *Process Saf. Environ. Protect.* 106 (2017) 309–318.
- [33] S. Yi, P. Lai, G. Ma, J. Pan, Z. Chen, Y. Qin, X. Jiang, Green and facile synthesis of nanostructured Co<sub>3</sub>O<sub>4</sub>/CeO<sub>2</sub> catalysts via a glucose-urea method for NO oxidation, *Appl. Surf. Sci.* 626 (2023) 157180.
- [34] S. Zinatloo-Ajabshir, M. Emsaki, G. Hosseinzadeh, Innovative construction of a novel lanthanide cerate nanostructured photocatalyst for efficient treatment of contaminated water under sunlight, *J. Colloid Interface Sci.* 619 (2022) 1–13.
- [35] D.V. Pinjari, A.B. Pandit, Room temperature synthesis of crystalline CeO<sub>2</sub> nanopowder: advantage of sonochemical method over conventional method, *Ultrasound. Sonochim.* 18 (2011) 1118–1123.
- [36] M. Vatanparast, L. Saedi, Sonochemical-assisted synthesis and characterization of CeO<sub>2</sub> nanoparticles and its photocatalytic properties, *J. Mater. Sci. Mater. Electron.* 29 (2018) 7107–7113.
- [37] I.D. Yadav, A. Ansari, D. Yadav, S.S. Garje, Facile synthesis of CeO<sub>2</sub> nanoparticles and their applications in photodegradation of methylene blue and as supercapacitor electrode material, *Bull. Mater. Sci.* 46 (2023) 86.
- [38] A. Abbasi, H. Khojasteh, M. Hamadanian, M. Salavati-Niasari, Normal spinel CdCr<sub>2</sub>O<sub>4</sub> and CdCr<sub>2</sub>O<sub>4</sub>/Ag nanocomposite as novel photocatalysts, for degradation of water contaminants, *Separ. Purif. Technol.* 195 (2018) 37–49.
- [39] W. Zhang, J. Guo, X. Lv, F. Zhang, Combined machine learning and high-throughput calculations predict heyd–scuseria–ernzerhof band gap of 2D materials and potential MoSi<sub>2</sub>N<sub>4</sub> heterostructures, *J. Phys. Chem. Lett.* 15 (2024) 5413–5419.
- [40] S. Singh, S.-L. Lo, Single-phase cerium oxide nanospheres: an efficient photocatalyst for the abatement of rhodamine B dye, *Environ. Sci. Pollut. Control Ser.* 25 (2018) 6532–6544.
- [41] S. Saitzek, J.-F. Blach, S. Villain, J.-R. Gavarri, Nanostructured ceria: a comparative study from X-ray diffraction, Raman spectroscopy and BET specific surface measurements, *Phys. Status Solidi 205* (2008) 1534–1539.
- [42] V.G. Baldovino-Medrano, V. Niño-Celis, R. Isaacs Giraldo, Systematic analysis of the nitrogen adsorption–desorption isotherms recorded for a series of materials based on microporous–mesoporous amorphous aluminosilicates using classical methods, *J. Chem. Eng. Data* 68 (2023) 2512–2528.
- [43] K.S.W. Sing, R.T. Williams, Physisorption hysteresis loops and the characterization of nanoporous materials, *Adsorpt. Sci. Technol.* 22 (2004) 773–782.
- [44] L. Kuang, Y. Zhao, W. Zhang, S. Ge, Roles of reactive oxygen species and holes in the photodegradation of cationic and anionic dyes by TiO<sub>2</sub> under UV irradiation, *J. Environ. Eng.* 142 (2016) 04015065.
- [45] I. Mahboob, I. Shafiq, S. Shafique, P. Akhter, M. Hussain, Y.-K. Park, Effect of active species scavengers in photocatalytic desulfurization of hydrocracker diesel using mesoporous Ag<sub>3</sub>VO<sub>4</sub>, *Chem. Eng. J.* 441 (2022) 136063.
- [46] W.A. Al-Onazi, M.H. Ali, Synthesis and characterization of cerium oxide hybrid with chitosan nanoparticles for enhancing the photodegradation of Congo Red dye, *J. Mater. Sci. Mater. Electron.* 32 (2021) 12017–12030.
- [47] N. Daneshvar, D. Salari, A. Khataee, Photocatalytic degradation of azo dye acid red 14 in water on ZnO as an alternative catalyst to TiO<sub>2</sub>, *J. Photochem. Photobiol. Chem.* 162 (2004) 317–322.
- [48] s. Senthil Kumar, K. Lellala, A. Mahalingam, P. Arumugam, S. Chinnappanadar, A. Rajendran, Green synthesis of CeO<sub>2</sub>–TiO<sub>2</sub> compound using Cleome chelidonii leaf extract for excellent photocatalytic activity, *J. Mater. Sci. Mater. Electron.* 29 (2018).
- [49] A. Phuruangrat, S. Thongtem, T. Thongtem, Microwave-assisted hydrothermal synthesis and characterization of CeO<sub>2</sub> nanowires for using as a photocatalytic material, *Mater. Lett.* 196 (2017) 61–63.
- [50] S. Issarapanacheewin, K. Wetchakun, S. Phanichphant, W. Kangwansupamonkon, N. Wetchakun, Efficient photocatalytic degradation of Rhodamine B by a novel CeO<sub>2</sub>/Bi<sub>2</sub>WO<sub>6</sub> composite film, *Catal. Today* 278 (2016) 280–290.
- [51] K. Hamidian, M. Sarani, S. Mohebbi, A. Najafidoust, A. Miri, Study of photodegradation performance of Zn-doped CeO<sub>2</sub> nanoparticles for wastewater contaminants remediation under visible light, *Appl. Organomet. Chem.* 37 (2023) e7114.